Effect of build orientation on fracture and tensile behavior of A357 Al alloy processed by Selective Laser Melting

João Teixeira Oliveira de Menezes[a,b], Enrique Mariano Castrodeza[a,b], Riccardo Casati[a,*]

[a] Department of Mechanical Engineering, Politecnico di Milano, Via G. La Masa 34, 20156, Milano, Italy

[b] Department of Metallurgical and Materials Engineering, COPPE/Federal University of Rio de Janeiro, CP 68505, 21941-972, Rio de Janeiro, RJ, Brazil

*Corresponding author, riccardo.casati@polimi.it

Abstract

Selective Laser Melting (SLM) is an additive manufacturing technology that allows producing components through local melting of a metallic powder bed using high-power laser beam in accordance with 3D digital CAD models. Cast Al-Si-Mg alloys are broadly used due to their good processability by SLM and mechanical properties. This work investigates the mechanical behavior of A357 aluminum alloy produced by SLM in the as built and artificially aged conditions. In particular, the tensile properties and fracture toughness of the alloy were investigated according to different specimen orientations on the build plate in the first case and different crack propagation planes in the second. In addition, microstructural and fractographic analyses were performed in order to investigate crack propagation paths and fracture mechanisms. The results showed that building orientation has a strong influence on material response, mainly with regards to the fracture toughness. The melt pool boundaries act as preferential paths for crack propagation and lead to a marked drop in fracture toughness of samples with cracks perpendicular to the building direction.

Keywords: Selective Laser Melting; A357 Al-alloy; Fracture toughness; C(T) specimens; *J*-R curves.

Introduction

Selective laser melting (SLM) is an Additive Manufacturing (AM) technology that allow producing parts with complex shape according to 3D digital models by layer-wise addition of material. SLM is based on local melting of a metal powder bed by high-power laser beam. Almost fully-dense functional and structural components are nowadays produced by SLM for service in industrial, aeronautical and medical applications using different gas-atomized alloys [1]-[3].

Among Al alloys, the Al-Si casting grades are the most used, since they are relatively easy to be processed, leading to parts without unacceptable microstructural defects. A357 is a heat treatable hypoeutectic Al-Si-Mg alloy showing good mechanical and corrosion performance, broadly used in casting of structural parts. The A357 alloy is mainly strengthened by $Mg_4Al_3Si_4$ coherent precipitates, known as β'', which form upon thermal aging from the aluminum supersaturated solid solution [4]-

[6]. Our recent work [7] revealed that A357 powder can be processed by SLM to produce high strength dense parts and that as built condition can be considered as fully appropriate for an effective dispersion strengthening process by artificial aging. In many alloys, indeed, the extremely high cooling rate involved in SLM leads to the formation of supersaturated solid solutions that can be exploited to form strengthening dispersoids by tailored heat treatments [7]-[11]. In particular, in A357 alloy processed by SLM, the highest yield and ultimate tensile strengths are exhibited when the material is aged at 160°C for 4 hours starting from the as built condition [7].

In this context, the present work investigates the fracture and tensile behaviors of the A357 aluminum alloy processed by SLM, in the as built and artificially aged condition. Particular attention has been given to the anisotropic behavior of the material. Tensile properties have been evaluated along the direction orthogonal and parallel to building direction, whereas fracture toughness tests were performed on specimens with three different crack plane orientations. Tensile mechanical properties were determined from engineering stress *vs.* strain curves, whereas fracture toughness was obtained through crack growth resistance curves (*J*-R curves) using the unloading compliance method. In order to investigate the crack path in the different crack plane orientations, microstructural and fractographic analyses were carried out using optical and electron microscopes.

Experimental procedure

Material and SLM process

Gas atomized A357 Al alloy powder was supplied by LPW South Europe Srl with size distribution within the range 20-63 μm and chemical composition reported in Table 1.

Table 1 - Chemical composition (weight fraction, %) of the investigated A357 Al powder.

Si	Mg	Fe	Cu	Mn	N	O	Al
6,5	0,58	0,1	< 0,05	< 0,1	< 0,2	0,1	Bal.

The powder was processed under Ar atmosphere by a Renishaw AM250 SLM system that uses a single mode pulsed-wave fiber laser. The process parameters were set as follow:

- Hatch distance = 115 μm
- Point distance = 80 μm
- Exposure time = 140 μs
- Focal point = 1 mm (above the powder bed)
- Layer thickness = 25 μm
- Power = 200 W

Samples for tensile and fracture toughness tests were produced using a meander scanning strategy and the scanning direction was rotated by 67° after each layer completion. According to our previous study [7], optimized isothermal aging was performed at 160 °C for 4 hours on as built samples to achieve maximum hardness of the material.

Tensile tests

Cylindrical dog-bone specimens for tensile tests having gauge length of 20 mm and diameter of 4 mm according to ASTM E8/E8M-16a standard [10] were machined from the printed bars with size 10 mm x 10 mm x 100 mm. Tensile specimens having longitudinal axis orthogonal and parallel to the building direction were named as Horizontal (H) and Vertical (V) sample, respectively, as shown in the schematic representation of Figure 1. Tensile tests were performed at room temperature by MTS Alliance RT/100 universal testing machine and by using an extensometer. The crosshead speed was set to 0.5 mm/min. Three H and three V specimens were tested for each of the following conditions: i) as built and ii) artificially aged to peak hardness (T5 temper).

Fracture tests

Fracture tests according to ASTM E1820-18 standard [11] were performed using C(T) specimens (W = 24.8 mm, B = 12.4 mm), as shown in Figure 1. Fatigue pre-cracking and fracture tests were carried out at room temperature, in air and using a MTS Landmark servo-hydraulic testing machine instrumented with a 25 kN load cell and a MTS 632.02F-20 fracture extensometer. Crack lengths were estimated by elastic unloading compliance method. The specimens were subjected to fatigue post-cracking to identify the stable crack growth region. The initial and final crack lengths were optically measured according to the 9-point average method described in BS 7448-1:1991 standard [12] in a Starret HE400 profile projector. Figure 1 shows the crack orientations of the tested specimens taking the building direction (H) and the building plane (T-L) as references. L and T directions were defined arbitrarily. Fracture specimens were named T-L, H-L and T-H according to the load direction (first letter) and the crack orientation (second letter) and they were tested in both the as-built (AB) and artificially aged (AA) conditions.

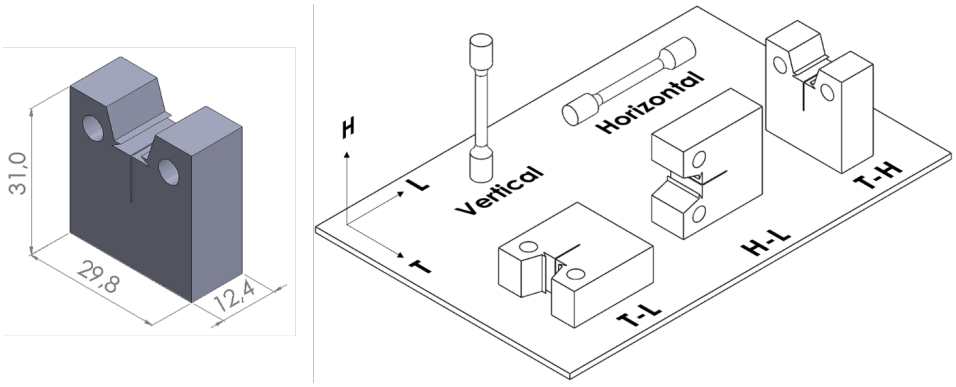

Figure 1 – Schematic depicting name and geometry of cylindrical dog-bone specimens for tensile tests and C(T) specimens for fracture toughness tests regarding the building direction (H) and building plane (T-L).

Microstructural and fractographic analyses

Microstructural and fractographic analyses were carried out by light optical microscope (LOM) and scanning electron microscope (SEM, mod. Zeiss EVO 50) equipped with energy dispersive X-ray analysis (EDX), secondary electrons and back-scattered electrons detectors. Samples for microstructure observations were prepared by standard grinding and polishing procedure. Chemical and electrolytic etching were performed using Keller's and Barker's reagents, respectively, in order to reveal microstructural features. Five polished sections of as built samples were used to obtain ten 25X micrographs that were computed by ImageJ and the achieved results were averaged. Fracture surfaces were inspected using SEM to observe the morphology of the fatigue pre-crack and the stable crack growth regions. To investigate the crack paths, C(T) specimens were cut at half the thickness and orthogonally to the crack propagation plane. The cut surfaces were subsequently grinded, polished and etched using Keller's solution.

Results

Tensile tests

In Figure 2, the stress-strain records of the as built and artificially aged A357 alloy are reported. As expected, AA specimens exhibit higher yield strength (σ_{YS}) and ultimate tensile strength (σ_{UTS}) than the AB counterparts. Moreover, the material shows an anisotropic behavior in both the conditions. Indeed, the Vertical specimens show lower σ_{YS} but higher σ_{UTS} than the Horizontal specimens, i.e. a more marked strain hardening. From the tensile curves the main mechanical properties were achieved and reported in Table 2.

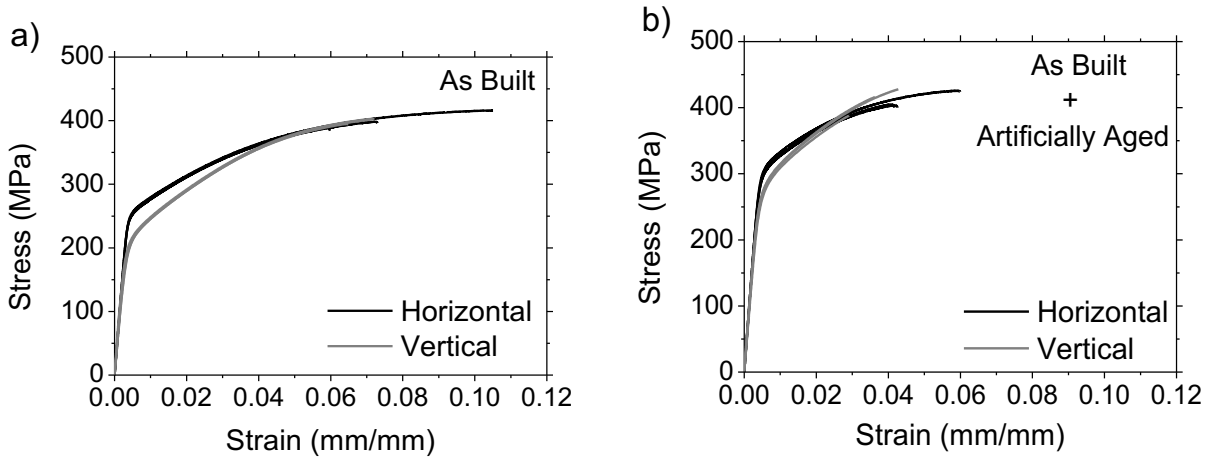

Figure 2 - Tensile curve of AB and AA A357 specimens printed horizontally and vertically with respect to the building direction.

Table 2 – Mechanical properties of the AB and AA A357 alloy.

Condition	Orientation	σ_{YS} [MPa]	σ_{UTS} [MPa]	Elongation [%]
AB	Horizontal	257 ± 3	398 ± 13	7.6 ± 1.8
	Vertical	216 ± 2	400 ± 04	6.9 ± 0.4
AA	Horizontal	309 ± 3	411 ± 10	4.8 ± 0.8
	Vertical	282 ± 1	411 ± 21	4.1 ± 0.4

Fracture tests

Figure 3a and Figure 3b show the *P*-CMOD records for C(T) specimens tested in the AB and AA conditions, respectively. The unloading-reloading sequences necessary for crack length measurement by elastic compliance are noticeable in the experimental records.

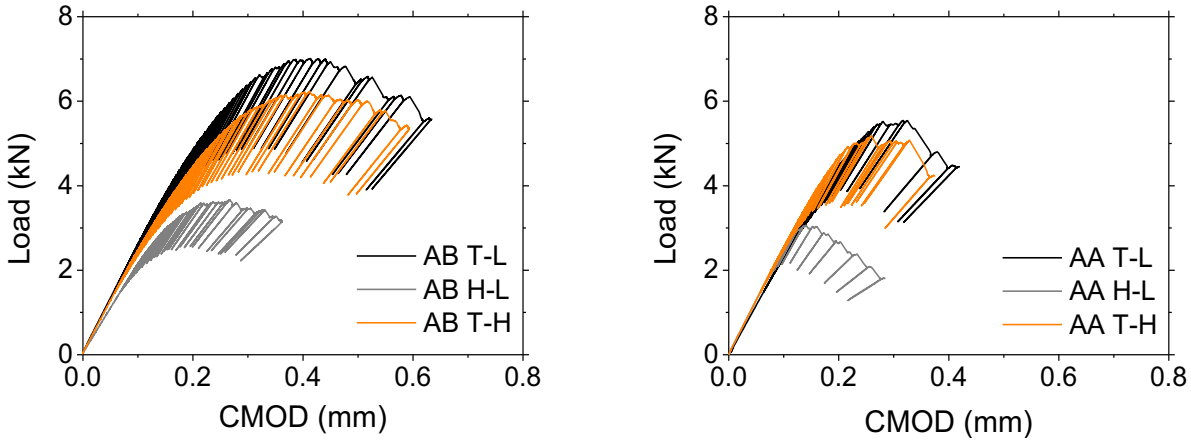

a) AB specimens b) AA specimens

Figure 3 – *P*-CMOD records for the AB and AA C(T) specimens notched in different orientations.

Fracture surfaces and crack length measurements

The fracture surfaces of all the C(T) specimens are shown in Figure 4. Fatigue pre-crack, stable crack growth and fatigue post-crack regions can be discernible in all cases.

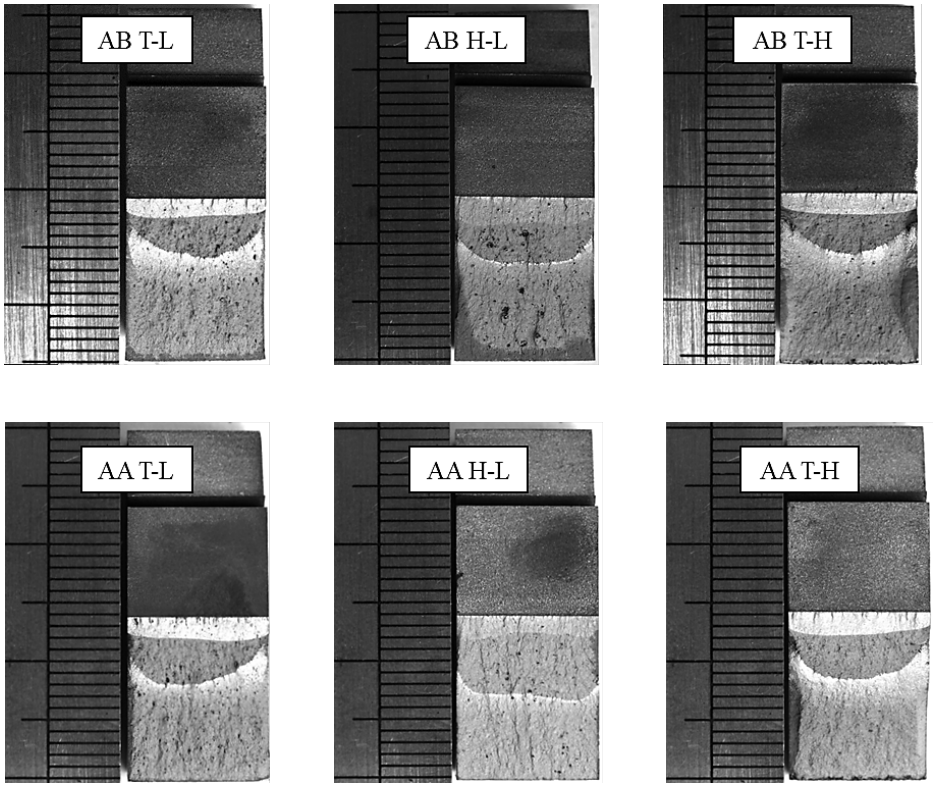

Figure 4 – Fracture surfaces of T-L, H-L and T-H C(T) specimens in the AB and AA conditions (left scale minor division: 1 mm).

Results of the physical crack length measurements are collected in Table 3. The physical crack extension (Δa), the crack extension estimated by elastic unloading compliance (Δa_{UC}), as well as their difference (%) are also reported in the same table.

Table 3 – Physical initial and final crack lengths and stable crack extension measured from fracture surface (Δa) and by elastic unloading compliance method (Δa_{UC}).

Condition	Orientation	a_0 [mm]	a_f [mm]	Δa [mm]	Δa_{UC} [mm]	Differ. [%]
AB	T-L	12.18	14.88	2.70	2.43	10.0
	H-L	13.04	15.92	2.88	2.52	12.5
	T-H	12.48	14.90	2.42	2.00	17.0
AA	T-L	12.56	15.61	3.05	2.60	15.0
	H-L	12.35	17.42	5.06	4.84	4.0
	T-H	12.48	15.61	3.14	2.58	18.0

Crack growth resistance curves and fracture toughness

The experimental J-Δa pairs obtained for the AB and AA specimens in the three different crack propagation orientations are shown in Figure 5. The blunting line, 0.15 mm and 1.5 mm exclusion

lines (EL) for qualifying J-Δa pairs according to ASTM E1820-18 were also plotted, as well as the 0.2 mm offset line (OL). The adjusted J-R curves from qualified J-Δa pairs can also be observed in the Figure 5. Initiation fracture toughness values (J_{Ic}) were determined from J-R curves according to ASTM E1820-18 standard, which defines this value as the intersection of the regression line (adjusted J-R curve) with the 0.2 mm offset line parallel to the blunting line. Table 4 presents the J_{Ic} values for all the tested specimens.

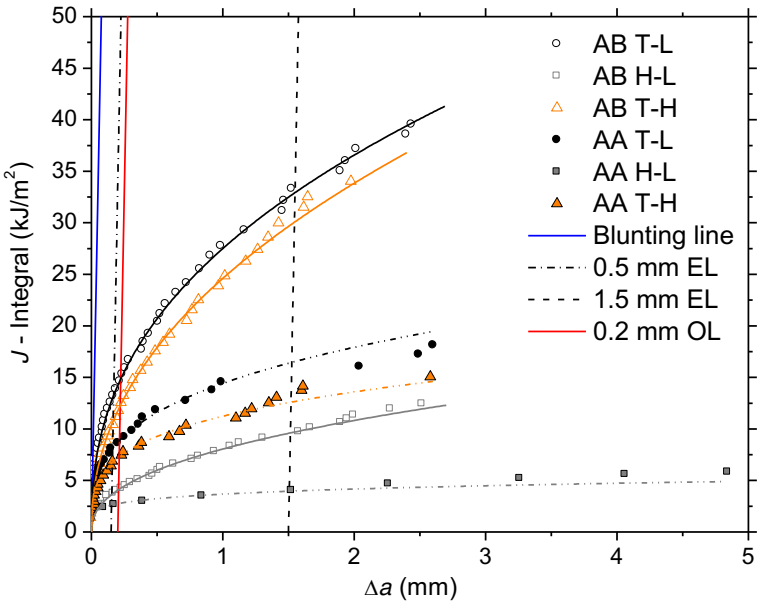

Figure 5 – Experimental J-Δa pairs and adjusted J-R curves for the A357 C(T) specimens in the AB and AA conditions.

Table 4 – Fracture toughness of the A357 specimens produced by SLM in AB and AA conditions.

Condition	Orientation	J_{Ic} [kJ/m²]
AB	T-L	14.83
	H-L	4.10
	T-H	12.23
AA	T-L	8.88
	H-L	2.75
	T-H	7.31

Microstructural analysis

Microstructural characterization of the AB alloy was carried out by LOM and SEM. Representative micrographs are depicted in Figure 6. The optical micrograph of a section parallel to the building direction shows solidification tracks that became visible after electrolytic etching in Barker's solution

(Figure 6a), which is commonly referred as fish-scale type microstructure. Refined grains are generated at track boundaries, whereas in the central regions of the beads, columnar grains competitively grown opposed to the direction of heat extraction. Former researches showed that grains with <001> direction parallel to the building direction favorably grow to the detriment of nearby grains [13]. In Figure 6b, the SEM image of the as built A357 alloy shows the cellular structure of grains, with primary Al cells decorated at boundaries by a Si network. The relative density of A357 samples fabricated by SLM was in average equal to 99.7% and no cracks were evident within the inspected samples.

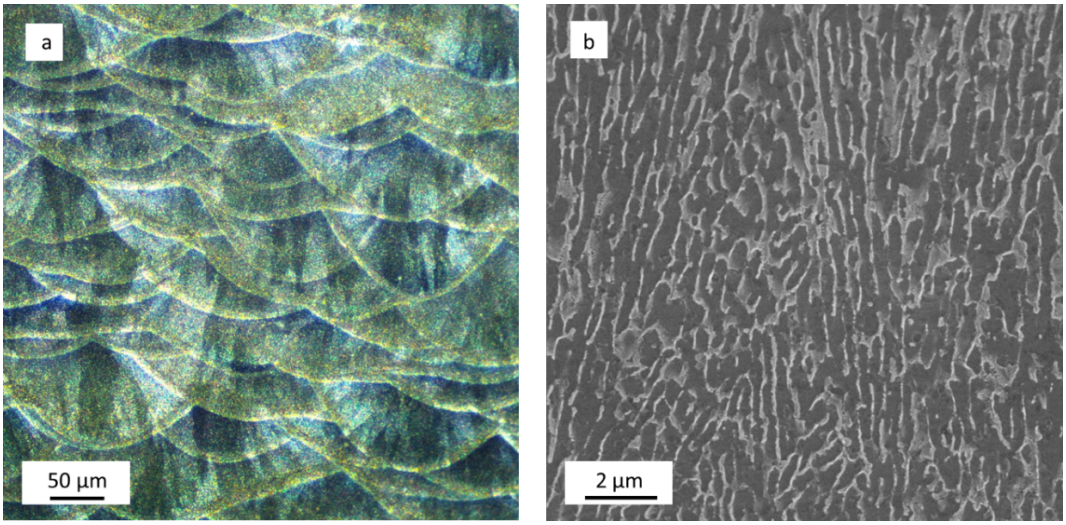

Figure 6 - Optical and SEM micrographs of as built A357 alloy. Both the images were taken from sections of samples parallel to building direction.

Fractographic analyses

Figure 7 shows representative LOM micrographs of the C(T) specimens taken from the mid-sections perpendicular to the crack plane in the region of stable crack growth after chemical etching with Keller's solution. These images show the crack paths according to the different crack propagation orientations.

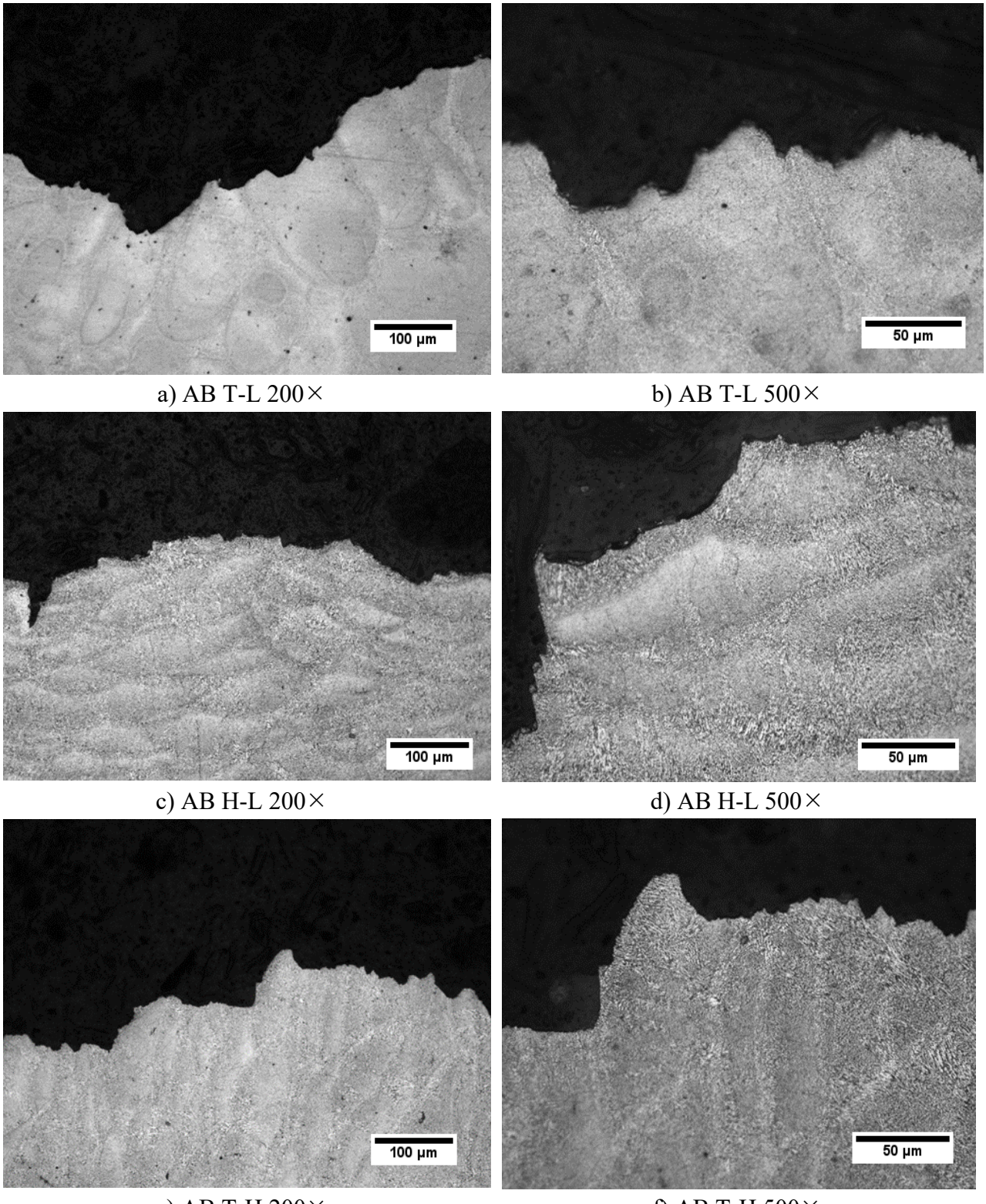

a) AB T-L 200×

b) AB T-L 500×

c) AB H-L 200×

d) AB H-L 500×

e) AB T-H 200×

f) AB T-H 500×

Figure 7 – LOM micrographs of C(T) specimens taken from the mid-sections perpendicular to the crack plane in the region of stable crack growth after chemical etching with Keller's solution.

Figure 8 to 9 show SEM images of the fracture surfaces of selected specimens. Figure 8 shows the fracture surface of the AB H-L specimen with a lower magnification. The notch, the fatigue pre-crack, and the stable crack growth are noticeable in the inferior, intermediate and superior regions,

respectively. Figure 9 shows the fracture surfaces of the fatigue pre-cracked region and the stable crack growth region of the AB H-L and the AA H-L C(T) specimens, and Figure 10 shows the stable crack growth regions of the C(T) specimens in the AB and AA conditions for the T-L and T-H orientations.

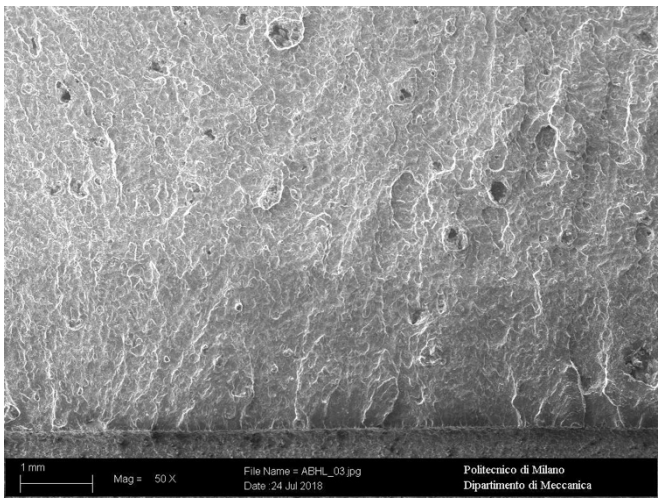

Figure 8 – Fracture surface image by SEM of the AB H-L specimen with a magnification of 50×. (notch + fatigue pre-crack + stable crack growth).

Fatigue pre-crack

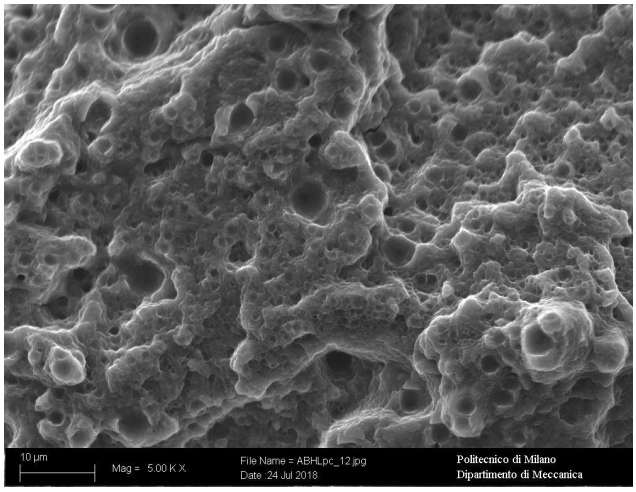

Stable crack growth

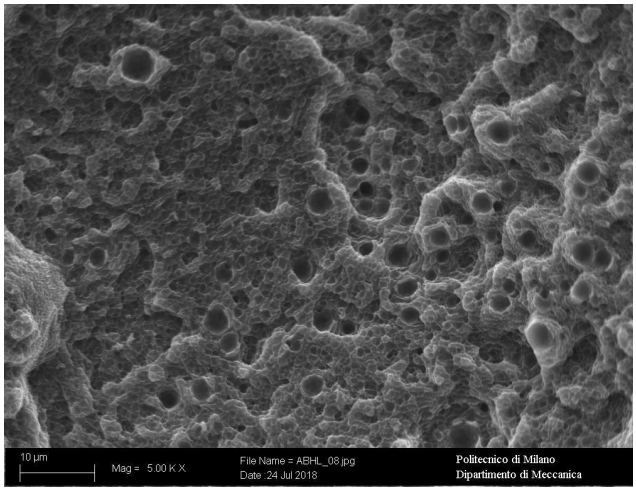

As built (AB)

Fatigue pre-crack

Stable crack growth

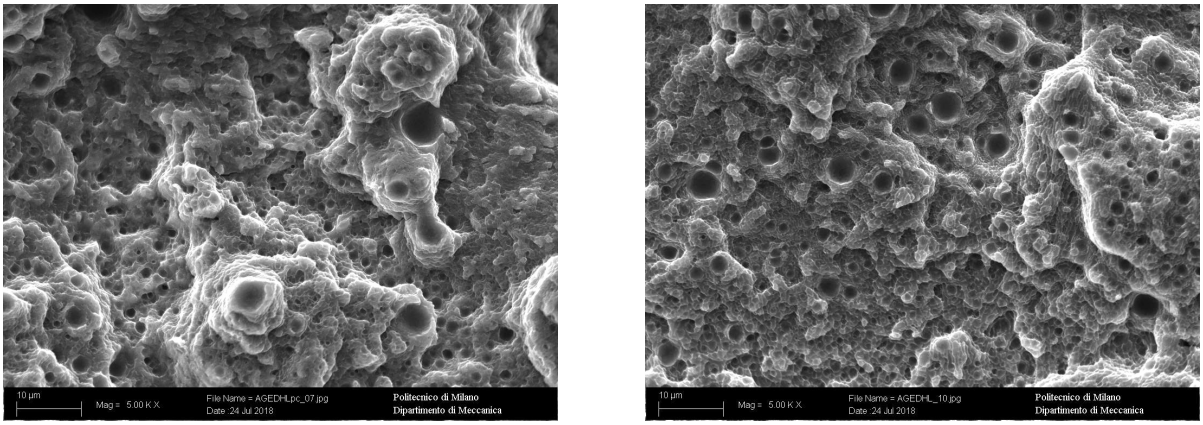

Artificially aged (AA)

Figure 9 – SEM images of the fracture surfaces of C(T) specimens in AB and AA conditions in the H-L orientation. Fatigue pre-crack surfaces are represented in the left and the stable crack growth surfaces in the right.

As built (AB) Artificially aged (AA)

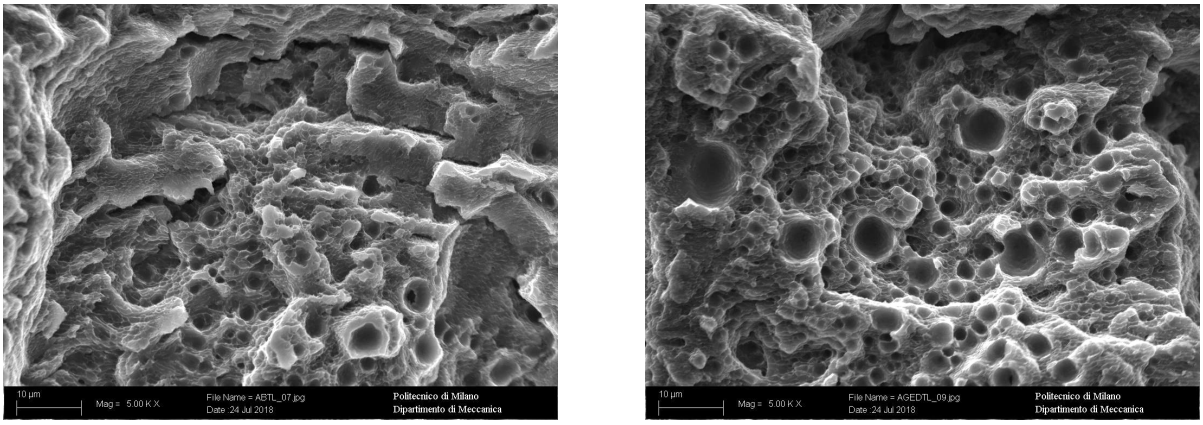

T-L orientation

As built (AB) Artificially aged (AA)

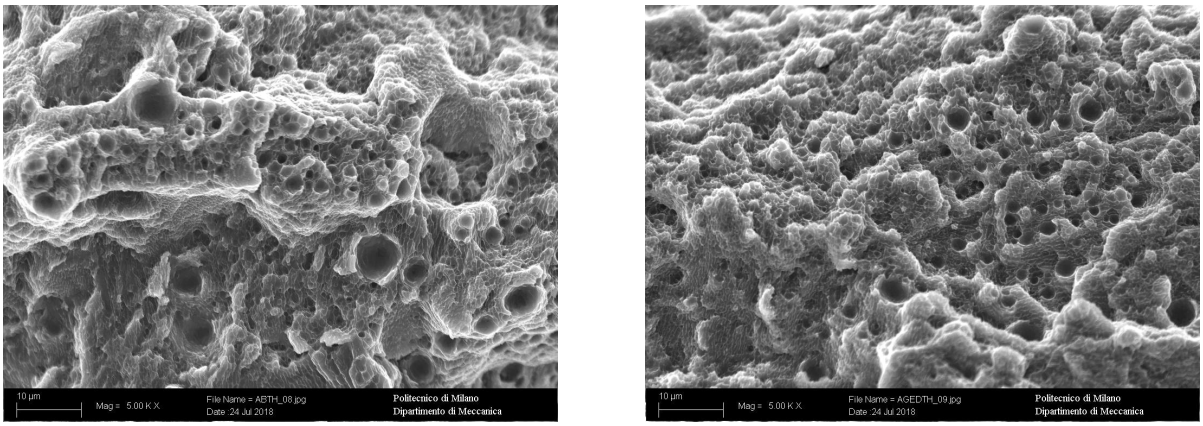

T-H orientation

Figure 10 – SEM images of stable crack growth regions of C(T) specimens in AB and AA conditions in the T-L and T-H orientation.

Discussion

A357 is an age hardenable Al alloy that is strengthened by $Mg_4Al_3Si_4$ coherent precipitates, known as β'', formed during artificial aging. The rapid solidification and cooling of the alloy from the SLM processing temperatures lead to the formation of a supersaturated solid solution [7][14]. This allow performing artificial aging right after the building process, thus by skipping the solution treatment (T5 temper). It has been shown in our previous study [7] that this alloy printed with identical combination of process parameters exhibits peak hardness when it is aged for 4 hours at 160 °C. Accordingly, the AA condition presented higher σ_{YS} values and lower ductility than the AB condition, both for the horizontal and vertical directions. On the other hand, if the comparison of the tensile properties is made according to specimen direction, the horizontally printed specimens presented higher strength and elongation at fracture values than those printed with longitudinal axis parallel to the building direction. The anisotropic behavior of the material under tensile loading can be reasonably ascribed to the formation of a crystallographic texture, as shown in previous works. Indeed, grains with the <001> directions parallel to the building direction, and therefore parallel to the maximum thermal gradient, favorably grow in Al alloys to the detriment of adjacent grains and give rise to the formation of crystallographic texture **Error! Reference source not found.**. In addition, the position of layer boundaries with respect to the loading direction is also considered a cause of the lower mechanical response of vertical samples, because high concentration of defects, e.g. oxides or small pores [15, 16].

Regarding the fracture behavior of the AB and AA A357 alloy, the T-L and the H-L specimens presented the highest and the lowest fracture toughness values, respectively. Those values dropped from 14.83 kJ/m² to 4.10 kJ/m² in the AB condition and from 8.88 kJ/m² to 2.75 kJ/m² in the AA condition. The fracture toughness of AB specimens is higher than those of the AA specimens in all the studied orientations.

Comparing the results on Table 2 and Table 4, it is important to note that the A357 alloy processed by SLM shows the typical trend of mechanical properties of conventional metallic materials: i.e. higher the yield strength, lower the fracture toughness. However, the toughness drop in H-L orientation is dramatic. A characterization of the mechanical properties based only on tensile testing of the material could lead to inappropriate conclusions. For the same orientation, the yield strength of AB specimens is approximately 75 to 85% that of the AA counterparts. In the same metallurgical state, the yield strength of the vertical printed specimens is approximately 85 to 90% that of horizontal printed ones. Contrarily, comparing fracture toughness values of specimens with the same crack orientation, it can be noticed that toughness of AA material corresponds to approximately 60 to 65% that of the AB alloys, and when the results of different orientations are compared for the same metallurgical conditions the gap reveals very large. The fracture toughness of the H-L specimens is as low as 28% that in the T-L ones.

These differences in fracture toughness were initially investigated by the observation of the fracture surfaces of the stable crack growth regions. Great differences in fracture toughness in metallic materials can be explained by the activation of different fracture micro-mechanisms, which generate different features on the fracture surfaces (like cleavage or quasi-cleavage surfaces or dimples) [17]. This approach was completely inadequate in this case. As can be seen from Figure 9 and Figure 10, the morphologies of the stable crack growth regions of different crack orientations and metallurgical

states do not present any remarkable difference. Additionally, it is practically impossible to distinguish fatigue from stable crack growth regions by SEM observations, as can be easily done in alloys processed by casting, rolling or another conventional process.

In order to understand the cause of the dramatic reduction in fracture toughness with the crack orientation, LOM micrographs of the crack paths were taken perpendicularly to the crack planes in the region of stable crack growth (Figure 7). As can be seen, in the T-L specimens crack propagates through solidified melt pools without following any specific path. In the H-L specimens, crack propagates preferentially through melt pool boundaries that are favorably oriented with respect to the crack plane. In the T-H specimens, cracks primarily propagate through solidified melt pools without following any specific path, but they change direction occasionally by following pool boundaries that, in this case, are not always oriented favorably with respect to the crack plane. For a better understanding of the phenomena, the crack paths for the three specimen orientations are schematically represented in Figure 11.

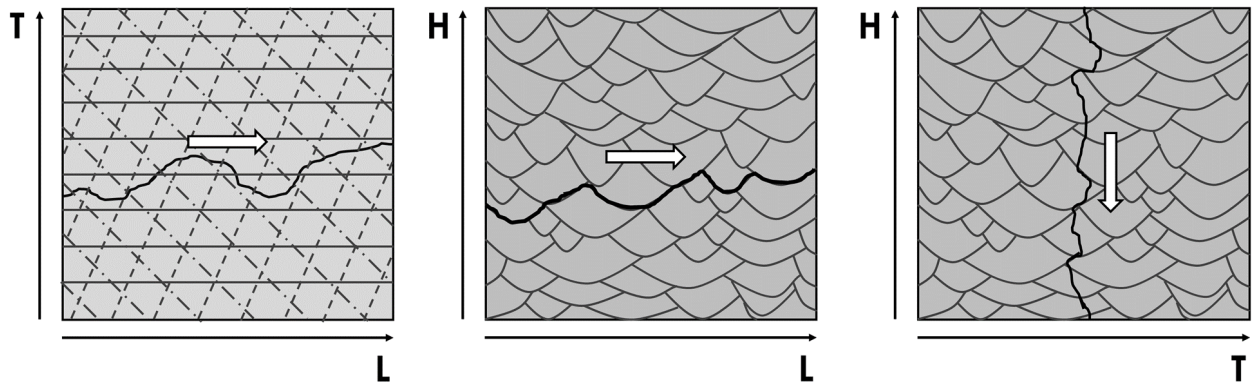

Figure 11 – Schematic representation of the crack paths. The arrows indicate crack propagation in the three analyzed orientations (from left to right: T-L, H-L, and T-H, respectively).

By comparing the fracture toughness values (Table 4) with the crack propagation paths (Figure 11), it can be inferred that the pool boundaries have a great effect on the fracture response of the material. The T-L specimens present the highest fracture toughness values and they show crack propagation that is minimally affected by the fish-scale microstructure generated by SLM processing. On the other hand, the H-L specimens show the lowest fracture toughness response and, accordingly, the cracks revealed propagating through an easy-path along pool boundaries. In the T-H specimens, which show intermediate fracture toughness values, cracks propagate predominantly through the solidified molten pools, with small deviations along weak boundaries.

Concluding remarks

This experimental work allowed collecting scientific and practical information that are necessary for the full exploitation of A357 parts produced by SLM in structural applications.

It can be inferred from collected data that both the building direction and the heat treatment have a remarkable effect on tensile properties of A357 Al alloy. In all cases the specimens printed with longitudinal axis perpendicular to the building direction showed higher yield strength than those printed with longitudinal axis parallel to the building direction. On the other hand, the yield strength of artificially aged specimens was higher than that of the as-built counterparts.

The effect of crack propagation orientation with respect to the building direction on fracture toughness is even more pronounced. In particular, a crack orthogonal to the building direction leads to a drastic drop in the material fracture toughness.

It was not possible to explain the differences in fracture toughness by SEM observations of the fracture surfaces. The morphologies of the stable crack growth regions of different crack orientations and metallurgical states did not present any remarkable difference. Indeed, it was practically impossible to differentiate even fatigue from stable crack growth regions by SEM observations.

LOM observations perpendicular to the crack plane in the stable crack growth region indicate that in the T-L specimens crack propagates through solidified melt pools without following any preferential path, whereas in the H-L specimens crack propagates preferentially through melt pool boundaries, that are favorably oriented with respect to the crack plane. In the T-H specimens, cracks primarily propagate through solidified melt pools, but they change direction occasionally by following pool boundaries. The dramatic loss in fracture toughness in the H-L orientation was attributed to this easy route for cracks to propagate.

Acknowledgments

The authors thank Mr. Cesar De La Cuesta for technical support and the Coordenação de Aperfeiçoamento de Pessoal de Nível Superior – Brasil (CAPES) that partially financed the study (Finance Code 001) through the scholarship of João Teixeira Oliveira de Menezes. This research work was also partially funded by EIT Raw Material within the framework of the project SAMOA - Sustainable Aluminium additive Manufacturing for high performance Applications.

References

[1] DebRoy, T., Wei, H. L., Zuback, J. S., Mukherjee, T., Elmerb, J. W., Milewskic, J. O., Beesea, A. M., Wilson-Heida, A., Ded, A., Zhange, W., Additive manufacturing of metallic components – Process, structure and properties, Progress in Materials Science, Volume 92 (2018), pp.: 112 - 224.

[2] Gu, D. D., Meiners, W., Wissenbach, K., Poprawe, R., Laser additive manufacturing of metallic components: materials, processes and mechanisms, International Materials Reviews, Volume 57 (2012), pp.: 133 - 164.

[3] Zhang, L.-C., Attar, H., Selective Laser Melting of Titanium Alloys and Titanium Matrix Composites for Biomedical Applications: A review, Advanced Engineering Materials, Volume 18 (2016), pp.: 463 - 475.

[4] American Society for Metals and ASM International. Handbook Committee. ASM Handbook: Nonferrous Alloys and Special-purpose Materials. Properties and Selection, Vol 2, ASM International, 1992.

[5] Zheng, Y.; Luo, B.; Bai, Z.; Wang, J.; Yin, Y. Study of the Precipitation Hardening Behavior and Intergranular Corrosion of Al-Mg-Si Alloys with Differing Si Contents. Metals 2017, *7*, 387.

[6] Ninive, P. H., Strandlie, A., Gulbrandsen-Dahl, S., Lefebvre, W., Marioara, C. D., Andersen, S. J., Friis, J., Holmestad, R., Løvvik, O. M., Detailed atomistic insight into the β" phase in Al-Mg-Si alloys, Acta Materialia, Volume 69 (2014), pp.: 126 – 134.

[7] Casati, R., Vedani, M., Aging Response of an A357 Al Alloy Processed by Selective Laser Melting, Advanced Engineering Materials (2018), pp.: 1 -7.

[8] Casati, R., Lemke, J., Vedani, M., Microstructural and Mechanical Properties of As Built, Solution Treated and Aged 18 Ni (300 grade) Maraging Steel Produced by Selective Laser Melting, La Metallurgia Italiana, Volume 109 (2017), pp.: 11 – 20.

[9] A. Saboori, A., Casati, R., Zanatta, A., Pavese, M., Badini, C., Vedani, M., Effect of graphene nanoplatelets on microstructure and mechanical properties of AlSi10Mg nanocomposites produced by hot extrusion, Powder Metallurgy and Metal Ceramics, Volume 56 (2018), pp.: 647 – 655.

[10] ASTM E8 / E8M-16a, Standard Test Methods for Tension Testing of Metallic Materials, ASTM International, West Conshohocken, PA, 2016.

[11] ASTM E1820-18, Standard Test Method for Measurement of Fracture Toughness, ASTM International, West Conshohocken, PA, 2018.

[12] BS 7448-1:1991, Fracture mechanics toughness tests – Part 1: Method for determination of K_{Ic}, critical CTOD and critical *J* values of metallic materials, BSI – British Standards Institution, London, 2002.

[13] Rao, J. H., Zhang, Y., Fang, X., Chen, Y., Wu, X., Davies, C.H.J., The origins for tensile properties of selective laser melted aluminium alloy A357, Additive Manufacturing, Volume 17 (2017), pp.: 113 - 122.

[14] Casati, R., Nasab, M. H., Coduri, M., Tirelli, V., Vedani, M., Effects of Platform Pre-heating and Thermal-Treatment Strategies on Properties of AlSi10Mg Alloy Processed by Selective Laser Melting, Metals 2018, 8 (11): 954.

[15] Casati, R., Lemke, J., Vedani, M., Microstructure an Fracture Behavior of 316L Austenitic Stainless Steel Produced by Selective Laser Melting, Journal of Materials Science & Technology, Volume 32 (2016), pp.: 738 – 744.

[16] Louvis, E., Fox, P., Sutcliffe, C. J., Selective laser melting of aluminium components, Journal of Materials Processing Technology, Volume 211 (2011), pp.: 275 – 284.

[17] Anderson, T. L., Fracture Mechanics: Fundamentals and Applications, Third edition, CRC Press, Boca Raton, FL (2005).